coatings

Article

Tribo-Behavior and Corrosion Properties of Welded 304L and 316L Stainless Steel

Hany S. Abdo [ID], Asiful H. Seikh *[ID], Hamad F. Alharbi [ID], Jabair Ali Mohammed [ID], Mahmoud S. Soliman [ID], Ahmed Fouly [ID] and Sameh A. Ragab

Mechanical Engineering Department, College of Engineering, King Saud University,
P.O. Box 800, Al-Riyadh 11421, Saudi Arabia; habdo@ksu.edu.sa (H.S.A.); harbihf@ksu.edu.sa (H.F.A.);
jmohammed@ksu.edu.sa (J.A.M.); solimanm@ksu.edu.sa (M.S.S.); amohammed7.c@ksu.edu.sa (A.F.);
sragab@ksu.edu.sa (S.A.R.)
* Correspondence: aseikh@ksu.edu.sa

Abstract: The present study investigates the electrochemical corrosion response and tribo-behavior of 304L and 316L stainless steel welded by gas metal arc welding (GMAW), which offered a high deposition rate. During this research, the metallurgically prepared welded samples were subjected to a tribological test and a corrosion test. The wear results were favorable for 316L steel, and it showed a lower coefficient of friction than the 304L specimen. These samples also underwent characterization studies, such as X-ray diffractometry (XRD) and scanning electron microscopy (SEM), to identify the different phases obtained on the cooling of the weld pool. Finally, both specimens were compared against their mechanical properties. Owing to the above properties, the 316L sample showed lasting durability, as compared to the 304L steel. The primary compositional difference is the higher presence of molybdenum and chromium in the 316L steel, compared to the 304L stainless steel.

Keywords: tribo-behavior; corrosion; 304L; 316L stainless steel; characterization

1. Introduction

The 304L steel belongs to the 304 series stainless steel. These steels are very versatile in their application and hence are one of the most vastly used kinds of stainless steel. This steel was formerly known as 18/8 stainless steel. This is due to the presence of chromium (18%) and nickel (8%). These steels, due to their high ductility and malleability, can be deep-drawn. Hence, these austenitic steels are used for utensils, springs, nuts and bolts, sanitary ware, troughs, architecture paneling, etc. The 304L steel is a low-carbon steel with improved weldability [1,2].

The 304L shows excellent resistance to a variety of corrosive environments. However, temperatures higher than 60 °C may cause SCC (stress corrosion cracking). These steels, being primarily austenitic, are capable of resisting oxidation even up to 870 °C. These steels are also able to resist carbide precipitation. On cold-working, these steels readily work-harden. Intermediate annealing alleviates the stresses induced due to the cold-working. This helps with avoiding tears and crack formations. These steels also show good machinability if the cutting tools are sharp and the proper chip formation is ensured. The machining of these steels requires coolants and lubricants. The weldability of these steels is excellent. Annealing is required for large welding sections to remove the unwanted residual stress that may have been induced due to the expansion–contraction occurring during the melting and solidification of the weld zone [3,4].

The 316L stainless steel has excellent mechanical properties and corrosion resistance. Therefore, these steels are used in medical implants. Dental implants, coronary stents, and orthopedic implants are part of the uses of 316L steel. These implants are manufactured using a unique laser powder bed fusion (LPBF) process for medical use [5]. This procedure helps to achieve the enhanced tensile strength of the implant [6].

In a deteriorating environment, the 316L facilitates the dissolution of Fe^{2+}, Cr^{3+}, and Ni^{2+}, etc. [7,8]. Researchers studied the corrosion behavior of 316L stainless steel, and they found that 3D-printed steels were less vulnerable to pitting susceptibility, as compared to the wrought 316L stainless steel. H_2O_2 tends to weaken the corrosion resistance of 316L steel [9]. This is related to an increase in the release of Ni ions [10], which is due to the increased reactions between metal ions and strong oxidant H_2O_2 [11,12].

Chromium, iron, and molybdenum are more active than nickel, and oxidize preferentially to form a passive film [13]. Iron forms intermetallic phases, which are less stable than chromium phases. The degradation of passive films increases the concentration of chromium and iron ions [14,15]. The nickel-reduced stainless steel (SS) alloys show an effective resistance to allergies when used in medical implants, but their use is limited due to their magnetic properties and low corrosion resistance [16]. Hence, 316L steel is used as a substitute [17]. The passivation properties of the 316L stainless steel are further enhanced by the subgrains' refinement [18]. Despite many advanced properties, 316L is a relatively expensive material. As a result, in some circumstances, 316L is substituted with 304L to reduce the cost. 304L is a low-carbon austenitic stainless steel. These types of steel have good corrosion resistance in various environments [19]. Austenitic stainless steels have a wide spectrum of resistance to corrosion in a chemical environment due to the formation of a protective passive film on its surface. This film is very thin, essentially transparent, and self-healing. If it is damaged mechanically or chemically, it will reform very rapidly [20]. However, such passive films are susceptible to breakdown in the presence of chloride ions, causing pitting corrosion [21]. Pitting corrosion is a significant problem that results in pits that appear tiny on the surface but propagate deep through the metals. This type of corrosion is considered to be more dangerous than uniform corrosion. The corrosion rate of pitting corrosion is 10–100 times faster than uniform corrosion [22]. Its aggressiveness is due to the small size, high diffusivity, and strong anionic nature of chloride ions [23].

The purpose of this study is to address a knowledge gap in the evaluation of 316L stainless steel tribo-behaviour and corrosion resistance. Electrochemical measurements, surface analysis, and wear testing were employed, and the results were compared to better understand the two welded specimens (304L and 316L, respectively).

2. Materials and Methods

Plates that were 10 mm thick were welded together for both the 304L and 316L steel. Gas metal arc welding (GMAW) was used to weld the plates. The welding process was performed using a GMAW power source from Poney, Wenling, China. Argon was used as the shielding gas with a flow rate of 25 L/min. GMAW uses a 0.035-inch thick consumable metal wire. During the welding, a current of 100 A and an arc voltage of 20 V was used. The wire feed speed rate was kept constant, at 200 mm/min.

The wear specimens for 304L and 316L steel were prepared from welded samples, as illustrated in the schematics below. The specimens were machined such that the welded zone was in the center of the wear specimen. The samples were then polished using SiC emery papers of various grades. Finally, the samples were polished to a super fine finish with diamond paste (1 μm).

A pin-on-disc test apparatus (model: MMT 20, Micromatic Technologies, Bengaluru, India) was utilized in a dry sliding condition for the steel samples, according to ASTM G195 [24], to investigate its tribological properties. Three applied loads were selected to perform the wear test: 100 N, 50 N, and 10 N. Figure 1 shows a schematic diagram of the wear tester, while Figure 2 shows a schematic diagram of pin sample prepared from the welded joints.
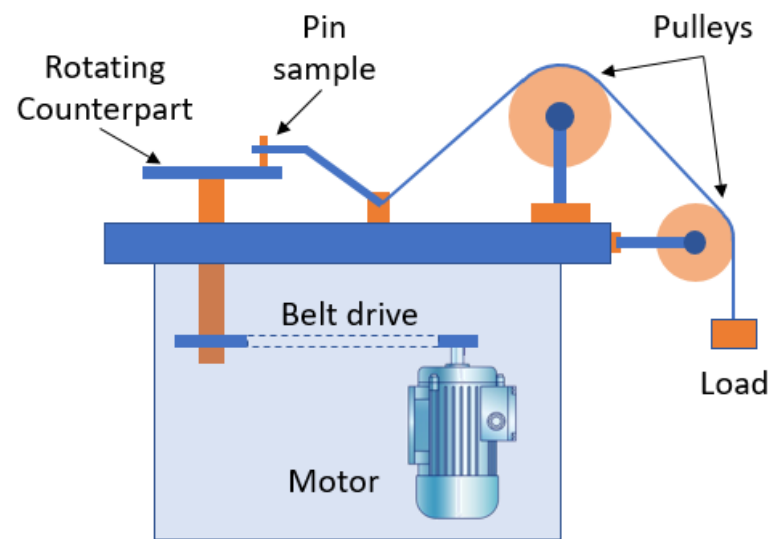
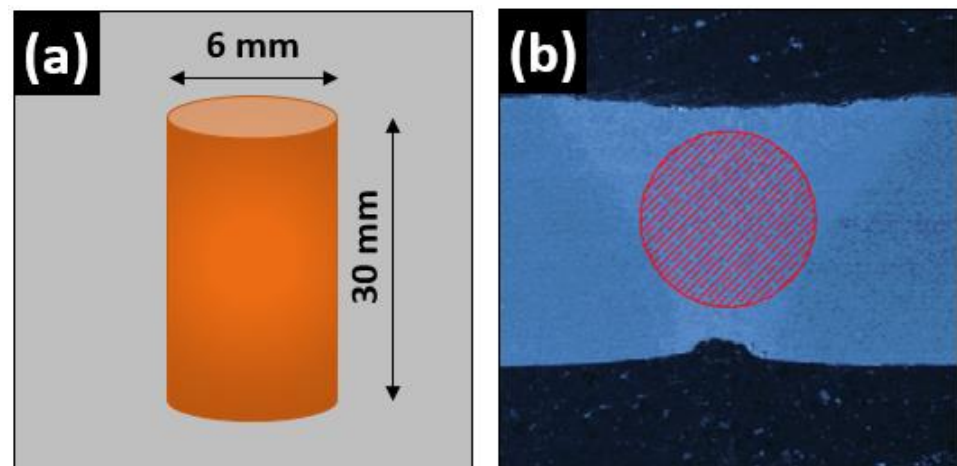**Figure 1.** Schematic diagram of tribo tester.

Figure 2. Schematic diagram of pin sample prepared from the welded joints; (**a**) sample dimensions and (**b**) cross-sectional area.

A square specimen (10 mm × 10 mm × 5 mm) was separately polished and prepared for the microstructural analysis. SEM micrographs were obtained via field emission scanning electron microscopy (FESEM) (model: JEOL JSM-7600F, Tokyo, Japan) with an attached unit for an energy-dispersive X-ray (EDX) analyzer. Images of varying magnification were obtained at a voltage of 10 kV using the secondary electrons (SE), while an EDX profile for an area spot was generated under 20 kV and high probe current of 9 mA.

The two steel types were characterized by the powerful X-ray diffraction (XRD) method. The XRD patterns were collected via employing a D-8 Discover (Bruker, Karlsruhe, Germany) diffractometer to identify the phase analysis. The XRD patterns were obtained at a 2/min scan rate, a 30 to 100° angle range, and a locked scan type at an increment of 0.02.

The potentiodynamic polarization test was performed on the samples using a three-electrode system (PGSTAT302N Autolab from Metrohm, Herisau, Switzerland) containing 3.5% NaCl (99% salt purity, delivered by Merck, Boston, MA, USA) as an electrolyte at room temperature. The saturated calomel electrode (SCE) served as a reference electrode, graphite served as the counter electrode, and the test sample served as the working electrode. All the experiments were performed in a potential range of −1 to 1 V vs. SCE at a scan rate of 1 mV/s. The samples were thoroughly polished with different grades of emery paper, followed by a cloth polisher. Before the final testing, the samples were ultrasonically cleaned using acetone and ethanol. The data was obtained from the polarization curve

by Tafel's extrapolation method. The surface area of the samples varied from sample to sample, but was normalized when plotted on the same sample area.

Electrochemical impedance spectroscopy was performed with the same instrument and solution as mentioned above. The impedance tests were performed utilizing a 100 mV AC voltage root-mean-square and 1 V DC voltage versus SCE in frequency ranges from 0.01 Hz to 300 kHz at 10 cycles for each decade. The total impedance and phase angles were estimated at every frequency. A Nyquist plot was obtained from the EIS experiment. The EIS data was obtained by proper fitting with an equivalent circuit model.

3. Results and Discussions

3.1. Microstructure and Energy-Dispersive X-ray (EDX)

The base metal of the samples of the 304L and 316L steel exhibited columnar microstructures, while the welded microstructure had a somewhat dendritic texture. A clear distinction between the dendritic and interdendritic areas is shown in the Figure 3. When the weld pool solidifies, solidification occurs through the formation of dendrites. There are two main structures observed in the microstructure of welding. One is a dendritic structure, and the other is an interdendritic structure [25]. EDS was used to differentiate these phases qualitatively, and the elemental concentrations are listed below. EDS is a qualitative analysis, and the data presented in Table 1 is primarily intended to distinguish the two stages and represents the actual composition of the elements present in the phases. The dendrite phase is austenite, whereas the interdendritic phase is δ-ferrite. The dendrites appear brighter, which may be due to the presence of a higher proportion of chromium [25,26].
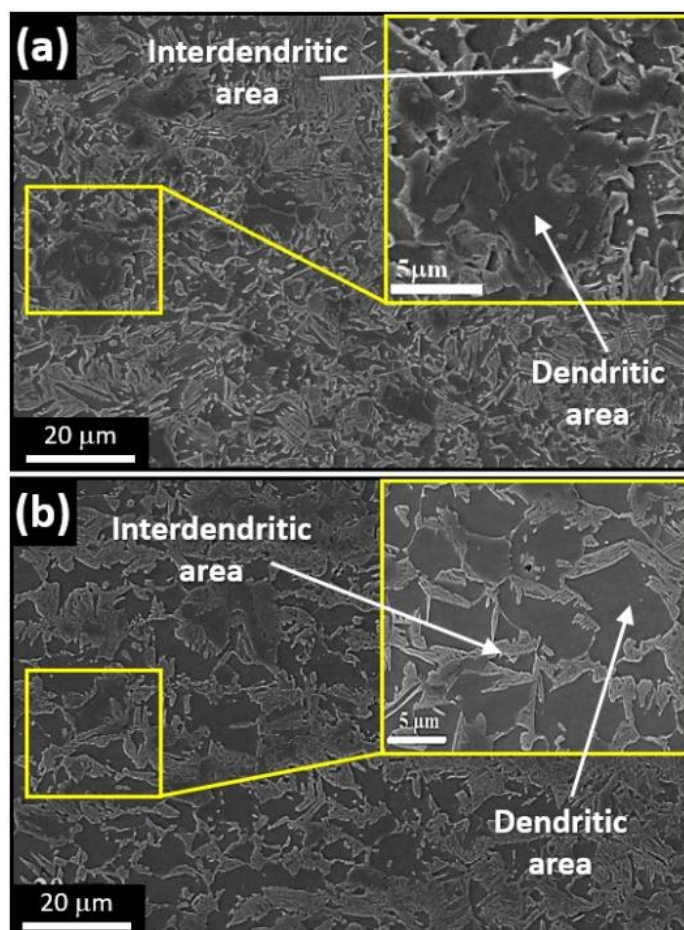

Figure 3. SEM images for a typical microstructure of welded (**a**) 304L stainless steel and (**b**) 316L stainless steel, showing a clear distinction between the dendritic and interdendritic areas.

Table 1. Elemental analysis in weight percentage (wt.%) of the 304L and 316L stainless steel used.

Material	C	Si	Mn	P	S	Cr	Mo	Ni	V	Fe
304L	0.0264	0.379	1.19	0.0211	0.003	18.23	0.0542	8.01	0.102	Bal
3016L	0.03	1.00	2.01	0.045	0.015	17.50	2.25	11.5	0.592	Bal

3.2. X-ray Diffractometry

The 304L welded and base metal exhibit typical XRD patterns where the primary peaks are of austenite (Figure 4). Since XRD is incapable of detecting the presence of a phase below 5%, δ-ferrite, which may be present in small amounts, is not detected. However, in the case of the weld zone, a combination of austenite and δ-ferrite is seen. The δ to γ transition occurs once the molten weld cools. In the case of GMAW, the cooling rate prevents the complete transformation of δ phase to γ phase, resulting in some δ-ferrite remaining in the weld [15]. A small amount of δ-ferrite has two advantages: first, it prevents hot cracking; second, as complete austenite, the weld is more susceptible to micro-fissures. Hence, the presence of δ-ferrite avoids this weld defect [15].
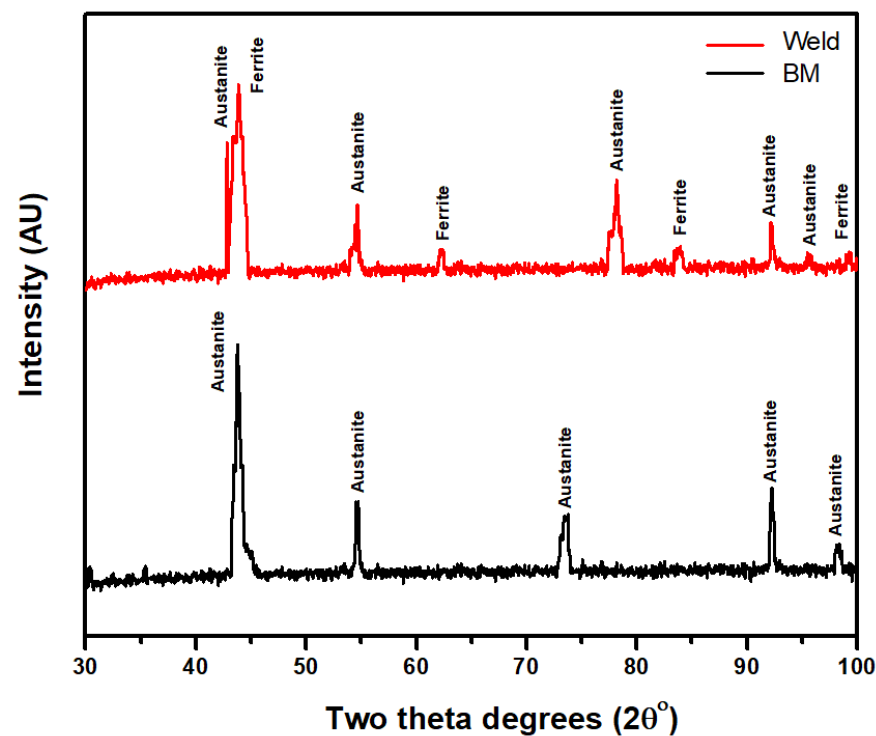
Figure 4. XRD pattern of 304L base metal (BM) and weldment (Weld).

The typical X-Ray pattern of 316L weldment shows the presence of austenite and ferrite (Figure 5). Some traces of intermetallic phases can be seen in the XRD patterns [27]. Furthermore, the SEM microstructure confirmed the presence of these phases. Similar transformations from the δ phase to γ phase occur for 316L weldments. However, due to the higher content of alloying elements, Mn and Cr intermetallics are also found in the weld zone of the 316L alloy elements. Cr_3C_7, Mn_3Ni_2Si, and Cr_3Si are the intermetallics identified in the XRD pattern.
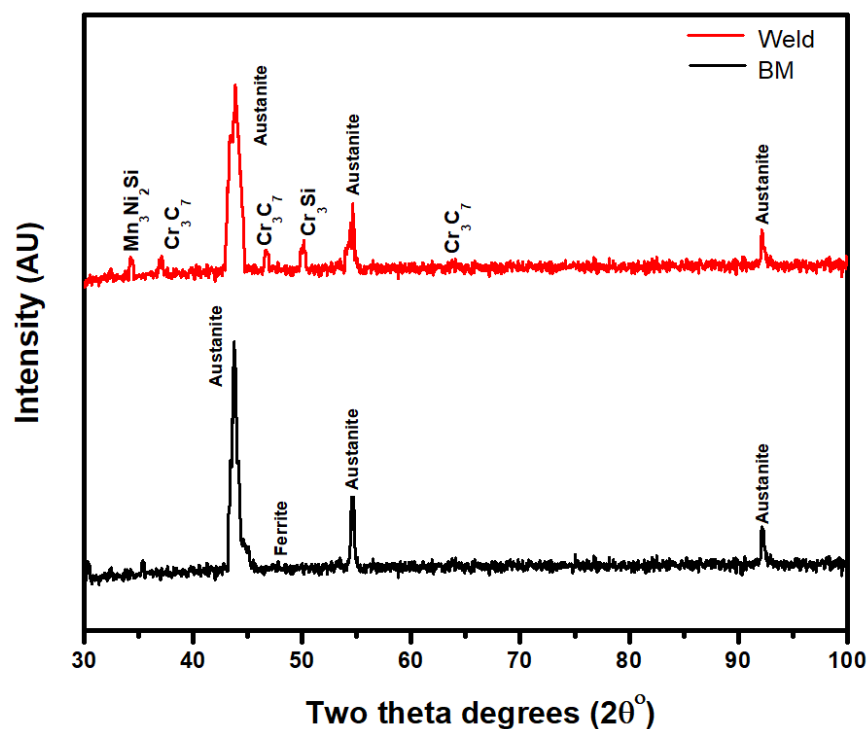
Figure 5. XRD pattern of 316L base metal (BM) and weldment (Weld).

3.3. Wear Behavior

The friction and wear responses of the 304L and 316L weldments were studied. The wear loss of the 304L and 316L specimens is depicted in Figure 6. When compared to the 304L sample, the 316L exhibits superior wear resistance. This can be due to the presence of higher alloying elements and the formation of intermetallic phases, which aid in the reduction of the specimen's coefficient of friction. This reduction in friction causes reduced abrasion between the sample and the EN31 counterpart disc, facilitating the reduction in material loss [28]. The samples were tested at different speeds and load conditions, as shown in Figure 6. The weight loss due to wear does not seem to be affected by the sliding speed. The wear, on the other hand, appears to be load-dependent. This is apparent because the friction force and contact area increase when irregularities merge under high loads [28]. This increases the loss of the sample material at higher loads.
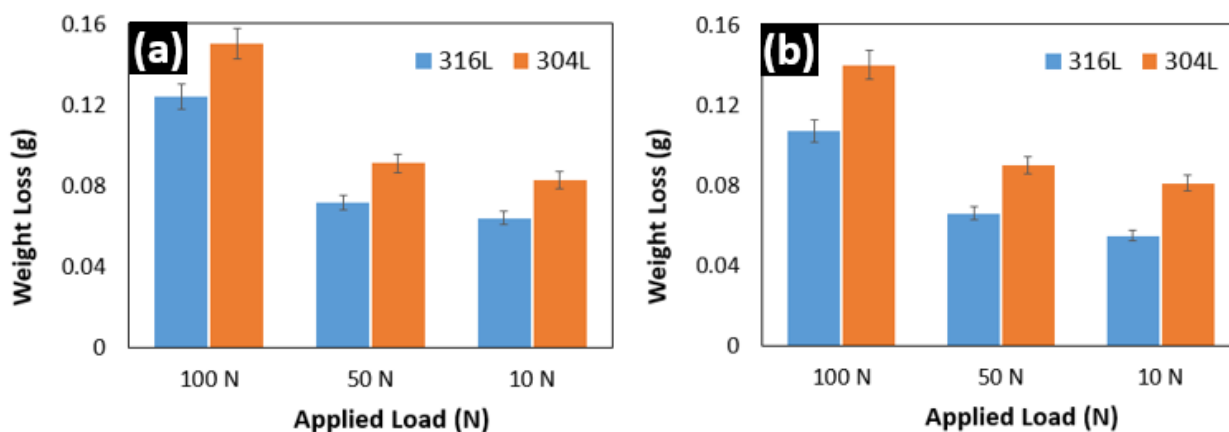

Figure 6. Weight loss at loads of 100 N, 50 N, and 10 N; (**a**) due to wear at rpm of 50, and (**b**) due to wear at rpm of 100.

Figure 6a shows the weight loss due to wear at 50 rpm, whereas Figure 6b shows the same at 100 rpm. The difference in the weight loss between the two RPMs is almost

negligible. This demonstrates that the sliding speed has little impact on the wear resistance of the material. Simultaneously, it is undeniable that the applied load has a considerable influence on the material's wear resistance. Many authors have reported that the wear mechanism is a combination of adhesion and abrasion [28].

3.4. Potentiodynamic Polarization Analysis

　　Figure 7 shows the potentiodynamic polarization of 316L SS and 304L SS samples in 3.5% NaCl solution. The i_{corr} and E_{corr} values of these two samples were obtained by Tafel's extrapolation method. Table 2 contains the data. From the data and the curve, it is clear that the 316L SS sample shows a lower i_{corr} value, i.e., a higher corrosion resistance. This is due to the natural passive layer formed on the surface of the 316L SS. On the surface of the 304L SS, a passive layer forms as well. However, the passive layer formed on the surface of the 316L sample is quite broad [29].
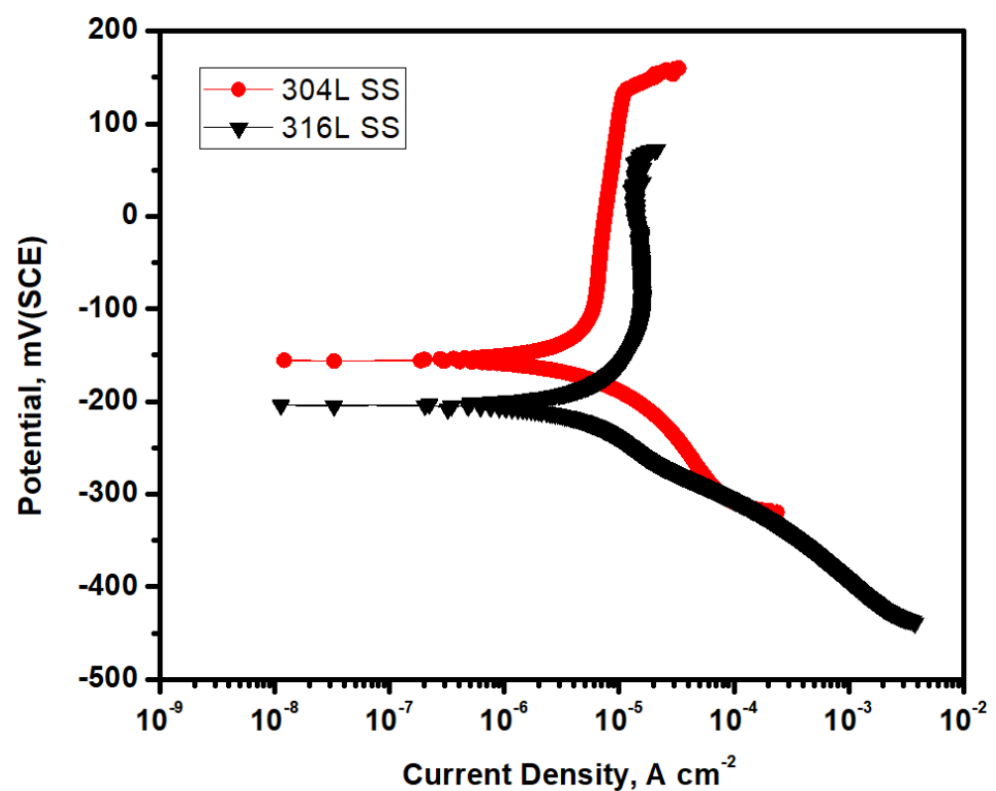

Figure 7. Potentiodynamic polarization curves of the 316L SS and 304L SS samples in 3.5% NaCl solution.

Table 2. Potentiodynamic polarization data.

Sample	Corrosion Current Icorr (A/cm^2)	Corrosion Potential Ecorr (V vs. SCE)	Anodic Slope βa (V dec^{-1})	Cathodic Slope βc (V dec^{-1})
316L SS	4×10^{-7}	-0.250	0.53261	-0.18204
304L SS	8×10^{-7}	-0.350	1.87781	-0.21404

3.5. Electrochemical Impedance Spectroscopy Analysis

　　The EIS data was obtained by proper fitting using the electrochemical equivalent circuit. In the circuit, some electrical elements represented the condition on the surface of samples. Those are solution resistance (Rs), polarization resistance (Rp), double layer capacitance (CPE/Cdl), and constant phase element (Q). The Rs value is affected by the environment, the samples' position, etc. Therefore, Rs cannot be used as a representation of the corrosion resistance of samples. However, the value of Rp is influenced only by the material. Thus, Rp is used to represent the of corrosion resistance of the sample. There is a

linear relationship between the corrosion resistance of samples and the value of Rp [29]. Table 3 contains obtained EIS data. The Nyquist plot of the 316L SS and the 304L SS in 3.5% NaCl solution is given in Figure 8. From the figure, it is obvious that the pattern of the two curves is quite similar, and that they are close to each other. Although, the 316L stainless steel sample shows a higher impedance compared to the other one. The 316L stainless steel contains an additional 2% molybdenum, which facilitates the formation of a stronger and stable passive layer [29–32]. For this strong passive layer, the 316L stainless steel shows a better corrosion resistance property than the 304L stainless steel.

Table 3. EIS data of the 316L SS and the 304L SS in 3.5% NaCl solution.

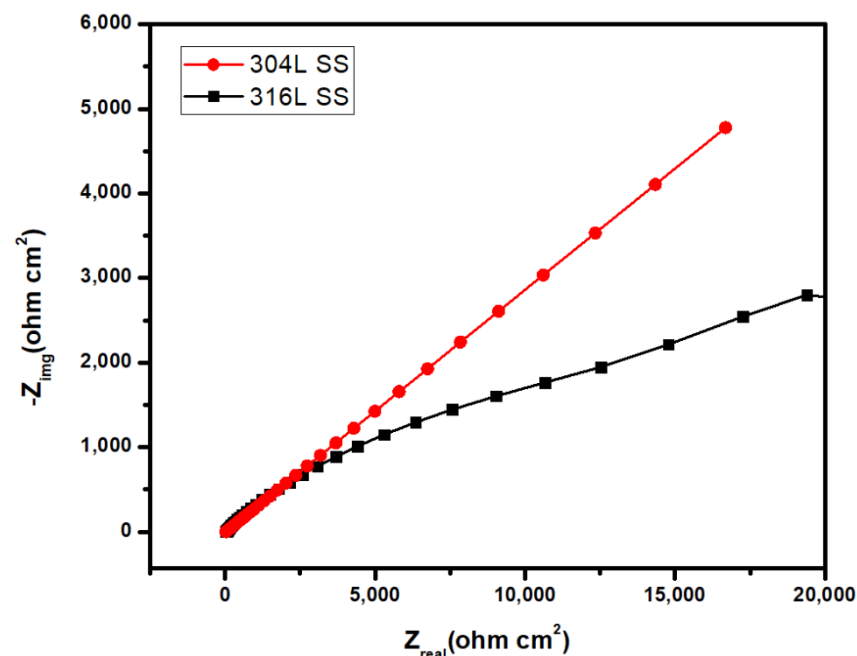| Sample	Rs ($\Omega \cdot cm^2$)	Rp ($k\Omega \cdot cm^2$)	CPE (Y, S s^n cm^{-2})	n
316L SS	8.09	5.57	178	0.68
304L SS	14.8	6.21	90	0.89

Figure 8. Nyquist plot of the 316L SS and the 304L SS in 3.5% NaCl solution.

4. Conclusions

The present research conducted shows a clear comparison of the 304L and 316L steels. The comparison based on the microstructure, wear behavior, and corrosion test show a clear contrast between the two steels:

- The wear resistance of the 316L welded steel is comparatively more than the 304L steel;
- The wear behavior is a mixture of adhesive and abrasive wear;
- The XRD pattern revealed the presence of delta iron in the 304L welded steel;
- In the case of the 316L welded steel, several intermetallic phases were observed which were formed due to the higher presence of the alloying elements.

The corrosion resistance property of both of the alloys was studied in 3.5% NaCl solution through the potentiodynamic polarization method and EIS analysis. In both cases, the 316L sample shows a better corrosion resistance property and surface resistance property.

References

1. Abdo, H.S.; Seikh, A.H. Mechanical Properties and Microstructural Characterization of Laser Welded S32520 Duplex Stainless Steel. *Materials* **2021**, *14*, 5532. [CrossRef]
2. Abdo, H.S.; Seikh, A.H. Role of NaCl, CO_2, and H_2S on Electrochemical Behavior of 304 Austenitic Stainless Steel in Simulated Oil Industry Environment. *Metals* **2021**, *11*, 1347. [CrossRef]
3. Abdo, H.S.; Seikh, A.H.; Samad, U.A.; Fouly, A.; Mohammed, J.A. Electrochemical Corrosion Behavior of Laser Welded 2205 Duplex Stainless-Steel in Artificial Seawater Environment under Different Acidity and Alkalinity Conditions. *Crystals* **2021**, *11*, 1025. [CrossRef]
4. Abdo, H.; Samad, U.A.; Mohammed, J.; Ragab, S.; Seikh, A. Mitigating Corrosion Effects of Ti-48Al-2Cr-2Nb Alloy Fabricated via Electron Beam Melting (EBM) Technique by Regulating the Immersion Conditions. *Crystals* **2021**, *11*, 889. [CrossRef]
5. Kong, D.; Dong, C.; Ni, X.; Li, X. Corrosion of metallic materials fabricated by selective laser melting. *NPJ Mater. Degrad.* **2019**, *3*, 24. [CrossRef]
6. Sander, G.; Tan, J.; Balan, P.; Gharbi, O.; Feenstra, D.; Singer, L.; Thomas, S.; Kelly, R.; Scully, J.; Birbilis, N. Corrosion of Additively Manufactured Alloys: A Review. *Corrosion* **2018**, *74*, 1318–1350. [CrossRef]
7. Hoar, T. The production and breakdown of the passivity of metals. *Corros. Sci.* **1967**, *7*, 341–355. [CrossRef]
8. Sikora, E. Defining the passive state. *Solid State Ionics* **1997**, *94*, 141–150. [CrossRef]
9. Cieślik, M.; Reczyński, W.; Janus, A.M.; Engvall, K.; Socha, R.; Kotarba, A. Metal release and formation of surface precipitate at stainless steel grade 316 and Hanks solution interface—Inflammatory response and surface finishing effects. *Corros. Sci.* **2009**, *51*, 1157–1162. [CrossRef]
10. Zhao, Z.-H.; Sakagami, Y.; Osaka, T. Toxicity of hydrogen peroxide produced by electroplated coatings to pathogenic bacteria. *Can. J. Microbiol.* **1998**, *44*, 441–447. [CrossRef]
11. Xu, W.; Yu, F.; Yang, L.; Zhang, B.; Hou, B.; Li, Y. Accelerated corrosion of 316L stainless steel in simulated body fluids in the presence of H_2O_2 and albumin. *Mater. Sci. Eng. C* **2018**, *92*, 11–19. [CrossRef]
12. Fonseca, C.; Barbosa, M. Corrosion behaviour of titanium in biofluids containing H2O2 studied by electrochemical impedance spectroscopy. *Corros. Sci.* **2001**, *43*, 547–559. [CrossRef]
13. Shih, C.-C.; Su, Y.-Y.; Su, L.H.J.; Chang, M.-S.; Lin, S.-J. Effect of surface oxide properties on corrosion resistance of 316L stainless steel for biomedical applications. *Corros. Sci.* **2004**, *46*, 427–441. [CrossRef]
14. Lee, J.-B.; Kim, S.-W. Semiconducting properties of passive films formed on Fe–Cr alloys using capacitiance measurements and cyclic voltammetry techniques. *Mater. Chem. Phys.* **2007**, *104*, 98–104. [CrossRef]
15. Hua, Y.; Mohammed, S.; Barker, R.; Neville, A. Comparisons of corrosion behaviour for X65 and low Cr steels in high pressure CO_2-saturated brine. *J. Mater. Sci. Technol.* **2019**, *41*, 21–32. [CrossRef]
16. Navarro, L.; Luna, J.; Rintoul, I. Surface conditioning of cardiovascular 316l stainless steel stents: A review. *Surf. Rev. Lett.* **2016**, *24*, 1730002. [CrossRef]
17. Man, C.; Dong, C.; Liu, T.; Kong, D.; Wang, D.; Li, X. The enhancement of microstructure on the passive and pitting behaviors of selective laser melting 316L SS in simulated body fluid. *Appl. Surf. Sci.* **2018**, *467–468*, 193–205. [CrossRef]
18. Al-Mamun, N.S.; Deen, K.M.; Haider, W.; Asselin, E.; Shabib, I. Corrosion behavior and biocompatibility of additively manufactured 316L stainless steel in a physiological environment: The effect of citrate ions. *Addit. Manuf.* **2020**, *34*, 101237. [CrossRef]
19. Lippold, J.C.; Kotecki, D.J. *Welding Metallurgy and Weldability of Stainless Steels*; John Wiley & Sons: Hoboken, NJ, USA, 2005.
20. Fontana, M.G.; Greene, N.D. *Corrosion Engineering*, 2nd ed.; McGraw-Hill International Book Company: New York, NY, USA, 1978; p. 194.

21. Asaduzzaman, M.D.; Mustafa, C.M.; Islam, M. Effects of concentration of sodium chloride solution on the pitting corrosion behavior of AISI-304L austenitic stainless steel. *Chem. Ind. Chem. Eng. Q.* **2011**, *17*, 477–483. [CrossRef]

22. Darowicki, K. Evaluation of pitting corrosion by means of dynamic electrochemical impedance spectroscopy. *Sci. Direct Electrochim. Acta* **2004**, *49*, 2909–2918. [CrossRef]

23. Galvele, J.R. Transport process in passivity breakdown-II. Full hydrolysis of metal ions. *Corros. Sci.* **1981**, *21*, 551–579. [CrossRef]

24. Standard Guide G195. Standard Guide for Conducting Wear Tests Using a Rotary Platform Abraser. In *Annual Book of ASTM Standards*; ASTM: Philadelphia, PA, USA, 1994.

25. Abdo, H.; Seikh, A.; Mohammed, J.; Uzzaman, T. Ameliorative Corrosion Resistance and Microstructure Characterization of 2205 Duplex Stainless Steel by Regulating the Parameters of Pulsed Nd:YAG Laser Beam Welding. *Metals* **2021**, *11*, 1206. [CrossRef]

26. Abdo, H.S.; Seikh, A.H.; Mandal, B.B.; Mohammed, J.A.; Ragab, S.A.; Abdo, M.S. Microstructural Characterization and Corrosion-Resistance Behavior of Dual-Phase Steels Compared to Conventional Rebar. *Crystals* **2020**, *10*, 1068. [CrossRef]

27. Abdo, H.S.; Seikh, A.H.; Mohammed, J.A.; Luqman, M.; Ragab, S.A.; Almotairy, S.M. Influence of Chloride Ions on Electrochemical Corrosion Behavior of Dual-Phase Steel over Conventional Rebar in Pore Solution. *Appl. Sci.* **2020**, *10*, 4568. [CrossRef]

28. Fouly, A.; Almotairy, S.; Aijaz, M.; Alharbi, H.; Abdo, H. Balanced Mechanical and Tribological Performance of High-Frequency-Sintered Al-SiC Achieved via Innovative Milling Route—Experimental and Theoretical Study. *Crystals* **2021**, *11*, 700. [CrossRef]

29. Mesquita, T.J.; Chauveau, E.; Mantel, M.; Kinsman, N.; Nogueira, R.P. Influence of Mo Alloying on Pitting Corrosion of Stainless Steels Used as Concrete Reinforcement. *Rev. Esc. Minas* **2013**, *66*, 173–178. [CrossRef]

30. Jones, D.A. *Principles and Prevention of Corrosion*; Macmillan Publishing Company: New York, NY, USA, 1992; pp. 514–516.

31. Roberge, P.R. *Corrosion Engineering Principles and Practices*; McGraw-Hill International Book Company: New York, NY, USA, 2008; p. 190.

32. Roberge, P.R. *Handbook of Corrosion Engineering*; McGraw-Hill International Book Company: New York, NY, USA, 2000; pp. 723–727.